

Computation Kernel for Feynman Diagrams

Daria Gazizova,¹ Rayan Farid,¹ B. D. E. McNiven,^{2,3} I. Assi,¹ Ethan G. Armstrong,³ and J. P. F. LeBlanc^{1,3,*}

¹*Department of Physics and Physical Oceanography, Memorial University of Newfoundland,
St. John's, Newfoundland & Labrador, Canada A1B 3X7*

²*Faculty of Engineering and Applied Science, Memorial University of Newfoundland and Labrador,
St. John's, Newfoundland & Labrador, Canada A1B 3X5*

³*Compute Everything Technologies Ltd., St. John's, Newfoundland & Labrador, Canada*

(Dated: March 12, 2025)

We present a general representation for solving problems in many-body perturbation theory. By defining an overcomplete representation for the single-particle Green's function we show how one can convert an arbitrary Feynman graph to a universal kernel representation. Once constructed, the computation kernel contains no problem specific information yet contains all explicit temperature and frequency dependence of the diagram. This computation kernel is problem agnostic, and valid for any physical problem that would normally leverage the Matsubara formalism of many-body perturbation theory. The result of any diagram can be written as a linear combination of these computation kernel elements with coefficients given by a sum over products of known tensor elements that are themselves problem specific and represent spatial degrees of freedom. We probe the efficacy of this approach by generating the computation kernel for a low order self-energy diagram which we then use to construct solutions to distinct problems.

I. INTRODUCTION

The need for precise evaluation of correlated electron problems drives the development of numerous numerical approaches and serves as a catalyst for advancing quantum computational hardware and algorithms. Despite advancements in algorithms for quantum hardware, the need for purely classical approaches remains undiminished, as they have accounted for virtually all useful computations of correlated electron systems to date.[1, 2] On classical hardware, quantum algorithm development spans several research areas, including the study of equilibrium and non-equilibrium systems, methods for finite temperature and ground state properties, and approaches using wavefunctions versus correlation functions. All these avenues are worth pursuing, with the shared goal of solving challenging quantum systems on classical or quantum hardware.[3]

Among the methods for finite temperature systems in equilibrium is many-body perturbation theory that is formulated in terms of Feynman diagrams. While not a new concept, Feynman diagrams remain a cornerstone of computational physics and chemistry. In quantum chemistry, the lowest-order perturbations, Hartree-Fock theory, serve as the foundation for many approaches and can be formulated in terms of diagrams. Going beyond Hartree-Fock, diagrammatic methods are valuable not only due to their broad applicability but also for their potential to provide a path to finite-temperature results for dynamic properties while offering the flexibility to evaluate a variety of observables. These methods are, however, at least exponential in complexity as the order of the interaction increases,[4–6] and self-consistent approaches have shown evidence of false convergence[7–9].

At the same time there have been algorithmic advancements intended to drastically improve computation time. In the case of real and imaginary time representations, application of quantum tensor trains have shown promise for reducing the complexity of numerical problems by reducing expressions to tensor products[10–13]. Other alternate representations for Matsubara Green's functions show similar promise for application to diagrammatic problems[14–18]. In the case of problems formulated in the Matsubara frequency domain there are also symbolic approaches that have emerged and are able to generate analytic solutions to internal temporal degrees of freedom of arbitrary Feynman diagrams[19–22]. One such symbolic approach, algorithmic Matsubara integration (AMI), has been applied to a broad spectrum of problems[9, 22–31]. However, the AMI approach is currently limited in its application for a number of reasons. Computationally, the method suffers from a nearly factorial growth of the number of function calls required to evaluate diagrams of increasing order limiting applications to fifth or sixth order in practice[9, 29]. The method also requires access to the pole structure of the Green's function which prevents one from merging AMI with self-consistent schemes or applying AMI to systems with non-diagonal Green's functions.

Alternate representations of Green's functions provide a possible path forward for the AMI approach. In particular, the discrete Lehmann representation (DLR) is an alternate function representation for Matsubara Green's functions in both the imaginary time and imaginary frequency domains. The DLR represents the Green's function in imaginary frequency via a discretized spectral kernel wherein the pole structure is symbolically accessible and this allows one to merge the DLR with AMI to provide self-consistent schemes. This was recently shown to be effective for studying single-band impurity problems in both single-shot and self-consistent schemes.[32] There it

* jleblanc@mun.ca

was shown that an exponential trade-off in computational expense is accompanied by an exponential convergence of the result to the numerically exact result. However, applying this approach to multi-band or finite systems scales poorly due to the addition of yet another exponential computational scaling on top of existing factorial scalings.

In this work, we make substantial progress in applying the DLR combined with AMI to arbitrary systems beyond impurities such as multi-band problems or lattice problems. We consider the implications of applying the DLR to Feynman diagrams with additional internal spatial degrees of freedom and find that there is a factorizable component of the problem that is identical to the case of an impurity problem but depends only on the non-physical space of DLR poles. This realization allows us to rephrase the factorizable component as a kernel for systems with any set of internal spatial degrees of freedom. We call this factorizable component the computation kernel. Once the computation kernel is computed for a given diagram, it can be reused endlessly for new problems regardless of the spatial geometry of the system. We show that diagrams can be decomposed as a linear combination of computation kernel entries with coefficients that are a product of tensor elements that are *a priori* known from the DLR fit of the single-particle Green's function.

II. GENERAL METHODOLOGY

A. Discrete Lehmann Representation

This work relies heavily on the formulation of the discrete Lehmann representation (DLR) presented in Refs. [16, 33] for single particle Green's functions. The premise of the DLR is to approximate the spectral decomposition in the truncated form,

$$G(i\omega_n) = \int_{-\Lambda}^{\Lambda} K(i\omega_n, x)\rho(x)dx, \quad (1)$$

where ρ is the density and the kernel is given by $K(i\omega_n, x) = \frac{1}{i\omega_n - x}$ when represented in Matsubara frequencies, $i\omega_n$. In the frequency domain, the DLR procedure assigns a set of nodes along the imaginary axis, $\{i\omega_{DLR}\}$, that are determined uniquely for a given choice of Λ for a desired error tolerance at a chosen inverse temperature, β . The coefficients are selected such that the kernel is approximated with an error tolerance, ϵ , in the domain $[-\Lambda, \Lambda]$ based on fitting the discrete set of poles along the real axis, $\{x_\ell\}$. The Matsubara Green's function can then be approximated as a sum over a finite set of poles $\{x_\ell\}$ with weights A^ℓ as

$$G(i\omega_n) \approx G_{DLR}(i\omega_n) = \sum_{\ell=1}^r K(i\omega_n, x_\ell)A^\ell. \quad (2)$$

We pause to discuss an important biproduct of Eq. (2). Take for example a simple scenario of a non-interacting Green's function of a single pole, $G(i\omega_n, \epsilon) = \frac{1}{i\omega_n - \epsilon}$. Once we evaluate $G(i\omega_n, \epsilon)$ along the set of $\{i\omega_{DLR}\}$ frequencies, the DLR fit provides an approximation via the right-hand-side of Eq. (2) that no longer explicitly contains ϵ . Computationally, one is worse off in this scenario because of the replacement of a single physical simple pole, ϵ , with an entire set of auxiliary poles $\{x_\ell\}$. However, mathematically, the removal of ϵ from the problem provides a potential enormous advantage, allowing us to write very simple, yet general expressions for the evaluation of Feynman diagrams for arbitrary problems.

Once the set of A^ℓ coefficients are obtained, the Green's function can be used without knowledge of the physical pole that gave rise to the Green's function. One can view this as the replacement of a physical space of poles with a computational space that is problem agnostic and therefore identical for all problems.

B. Extending the DLR to Feynman Diagrams

Before deriving general expressions, we take a pedantic approach and walk through precisely what the DLR representation is doing for a sequence of problems of increasing complexity. To aid in this discussion, we turn the reader's attention to the schematic of Fig. 1. What we are depicting there is a sequence of problems of increasing complexity moving from top to bottom. The first scenario is the decomposition of a Matsubara Green's function of a physical state, ϵ , (depicted as a bar on the left) into a DLR representation[33, 34] of new auxiliary states x_ℓ (depicted as a set of bars on the right). This is what is described in Eq. (2), where a physical Green's function is now a sum over a non-physical space of non-interacting Green's functions with a set of coefficients, A^ℓ , as weights. Importantly, the non-physical states on the right, are no-longer explicitly dependent on the physical state ϵ .

If one can find an appropriate set of weights for the first problem, equivalent to a quantum impurity, then increasing the complexity of the physical space is straightforward. The second panel of Fig. 1 shows a set of physical eigenstates, ϵ_i , each of which may have its own frequency dependent Green's function. Using the DLR approach, one can sequentially project each physical Green's function into a fixed DLR basis. All that is required in doing so is tracking an additional index on the weight coefficients, A_i^ℓ for each of the ϵ_i eigenstates. Again, the non-physical states on the right are no-longer explicitly dependent on the physical eigenstates ϵ_i . Further, since we have chosen to project all of the physical states into a single fixed DLR basis, the mathematical representation of any choice of physical problem will now be mathematically identical and only the weight values will change.

Continuing the argument is straightforward for more complex problems. In the case of matrix-valued single

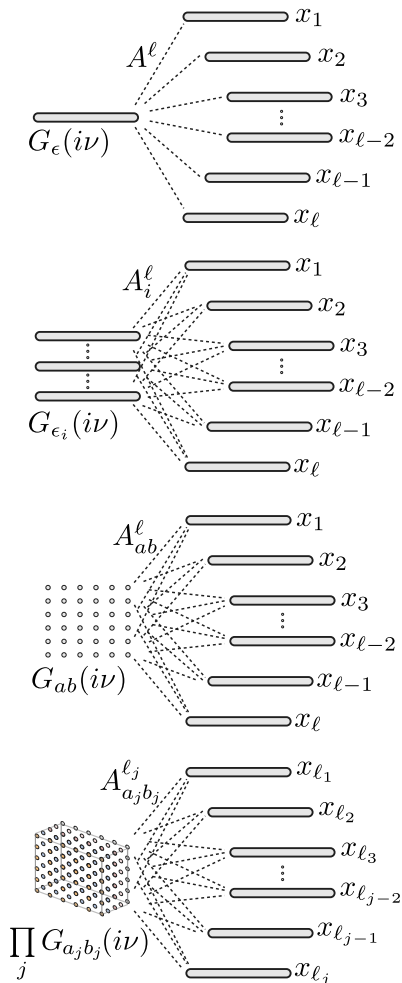


FIG. 1. Schematic representation of applications of a discrete Lehmann representation to increasingly complex datasets. From top to bottom these represent: an impurity Green's function, a diagonal Green's function, a matrix-valued Green's function, and a collection of Green's functions (as appear in Feynman diagrams). On the left of each schematic is a physical space of states while on the right is a particular basis of DLR poles, x_ℓ .

particle Green's function, G_{ab} , the usual DLR representation is applied and all matrix elements are assigned coefficients for the same set of x_ℓ poles. The storage of the necessary information requires a coefficient tensor that matches the geometry of the matrix representation

of the Green's function of the form A_{ab}^ℓ for Green's function elements $G_{ab}(i\omega_n) = \langle c_a^\dagger(\tau)c_b(0) \rangle$.

For the present work, we need to simultaneously store all information for Feynman diagrams that are at their core just collections of matrix-valued Green's functions as depicted in the bottom panel of Fig. 1. In this case, one can represent a collection of Green's functions, each with an index j , as $G^{(j)}$ either all in the same DLR representation or as a collection of unique representations by increasing the rank of the coefficient tensor. We generate a set of real-frequency DLR nodes for each of the j Green's functions, $\{x_{\ell_j}\}$, and then store their coefficients as $A_{a_j b_j}^{\ell_j}$. One can then represent a particular element of the j th Green's function in the DLR representation in the form,

$$G_{a_j b_j}(i\omega_n) = \sum_{\ell_j} \frac{A_{a_j b_j}^{\ell_j}}{i\omega_n - x_{\ell_j}}. \quad (3)$$

In the case that all DLR frequency nodes are the same this could be represented for all Green's functions via a single rank-4 tensor, $A_{j\ell ab}$. For technical reasons related to contour integration, we take the form of Eq. (3) and assume the entries of $\{x_{\ell_j}\}$ are all distinct. We note that our procedure is not a particularly novel use of the DLR approach, nor is it intended to be, and emphasize that it requires only repeated applications of existing DLR algorithms for matrix-value Green's functions.[33, 34]

C. Application to Feynman Diagrams

Having now established the notation for the replacement of Green's functions in a physical space with those in an arbitrary DLR representation we now move to the problem at hand of applying this to Feynman diagrams. Prior to applying the DLR form of the Green's function, a Feynman diagram is represented in a physical space of energy levels and is determined by a product Green's functions. Depending on the observable the diagram represents, there will typically be a number, m , independent labels, and, n , dependent labels. If one multiplies out the matrix-valued Green's functions, then a diagram is a high-dimensional summation over products of elements of those Green's functions. Focusing on a single term of such products, we define

$$H(\{i\nu_m\}, i\nu_x, \{a_j, b_j\}) = G_{a_1 b_1}(i\nu_1) \dots G_{a_m b_m}(i\nu_m) G_{a_{m+1} b_{m+1}}(\vec{\alpha}_1 \cdot \vec{\nu}) \dots G_{a_{m+n} b_{m+n}}(\vec{\alpha}_n \cdot \vec{\nu}), \quad (4)$$

where $\{i\nu_m\}$ is the set of internal Matsubara frequencies, $i\nu_x$, is one or more external Matsubara frequency, and the vector $\vec{\nu} = \{i\nu_1, \dots, i\nu_m, i\nu_x\}$ is defined such that the dot products $\vec{\alpha}_i \cdot \vec{\nu}$ represent an arbitrary linear combina-

tion of internal and external frequencies that depend on diagram topology.[22] With these simplifications, a particular diagram is then a summation of the independent Matsubara frequencies $i\nu_1 \rightarrow i\nu_m$ as well as a summation

over the relevant set of matrix indices $\{a_j, b_j\}$ which depends on diagram topology. One must also multiply each term in that sum by an appropriate product of interaction matrix elements which we denote for now as \bar{U} . For now, we treat the detailed interpretation of the summation over indices $\{a_j, b_j\}$ and detailed function dependence of \bar{U} as problem specific, and revisit in detail later.

A particular diagram topology \mathcal{D} will then contain terms in the form

$$\mathcal{D} = \sum_{\{\nu_m\}} \sum_{\{a_j, b_j\}} H(\{\nu_m\}, i\nu_x, \{a_j, b_j\}) \bar{U}, \quad (5)$$

$$\mathcal{D} = \sum_{\{\ell_i\}} \left[\underbrace{\sum_{\{\nu_m\}} \prod_{i=1}^m \frac{1}{i\nu_i - x_{\ell_i}} \prod_{j=1}^n \frac{1}{\vec{\alpha}_j \cdot \vec{\nu} - x_{\ell_{j+m}}}}_{\text{Exactly Solvable}} \sum_{\{a_j, b_j\}} \prod_{k=1}^{m+n} A_{a_k b_k}^{\ell_k} \bar{U} \right]. \quad (7)$$

We have underlined the exactly solvable part in Eq. (7). Specifically the Matsubara summation can be performed by hand for simple diagrams or automatically via algorithmic Matsubara integration (AMI).[35, 36] We proceed using AMI and will annotate for a specific diagram this quantity as

$$\mathcal{K}^{\mathcal{D}}(i\nu_x, \{\ell_i\}, \beta) = \sum_{\{\nu_m\}} \prod_{i=1}^m \frac{1}{i\nu_i - x_{\ell_i}} \prod_{j=1}^n \frac{1}{\vec{\alpha}_j \cdot \vec{\nu} - x_{\ell_{j+m}}}. \quad (8)$$

We emphasize the notational change to mark that $\mathcal{K}^{\mathcal{D}}$ is an explicit function of inverse temperature β after Matsubara summation. By substituting into Eq. (7) we obtain

$$\mathcal{D} = \sum_{\{\ell_i\}} \mathcal{K}^{\mathcal{D}}(i\nu_x, \{\ell_i\}, \beta) \sum_{\{a_j, b_j\}} \prod_{k=1}^{m+n} A_{a_k b_k}^{\ell_k} \bar{U}. \quad (9)$$

We can then replace the summation on the right with an appropriately indexed constant. We shift external parameters to indices and now specify also the diagram's dependence on those external properties on the left-hand side, which yields

$$\mathcal{D}(i\nu_x, \beta) = \sum_{\{\ell_i\}} \mathcal{K}_{i\nu_x, \beta}^{\mathcal{D}}(\{\ell_i\}) C_{\beta}^{\mathcal{D}}(\{\ell_i\}). \quad (10)$$

Equation (10) is a primary result of this paper. One can interpret the space of $\{\ell_i\}$ as a kernel for computing the diagram where $\mathcal{K}_{i\nu_x, \beta}^{\mathcal{D}}(\{\ell_i\})$ represents the kernel functions containing all frequency dependence while containing no problem specific information. The coefficients $C_{\beta}^{\mathcal{D}}(\{\ell_i\})$ contain all problem specific information, and while these coefficients depend implicitly on the inverse temperature, β , they do not depend on frequency

where we have, for now, suppressed the dependence of \mathcal{D} on external parameters. Our goal is to evaluate Eq. (5) and leverage the DLR representation. By simply replacing every Green's function with its own DLR representation from Eq. (3), we can rewrite Eq. (5) as

$$\mathcal{D} = \sum_{\{\ell_i\}} \sum_{\{\nu_m\}} \sum_{\{a_j, b_j\}} \prod_{i=1}^m \frac{A_{a_i b_i}^{\ell_i}}{i\nu_i - x_{\ell_i}} \prod_{j=1}^n \frac{A_{a_{j+m} b_{j+m}}^{\ell_{j+m}}}{\vec{\alpha}_j \cdot \vec{\nu} - x_{\ell_{j+m}}} \bar{U}. \quad (6)$$

We notice that there is a separable component that no longer contains problem specific information, but only the kernels of the DLR representations. We can therefore rewrite the expression as

and only depend explicitly on the $A_{a_k b_k}^{\ell_k}$ coefficients and the interaction matrix elements. Both the kernel entries, $\mathcal{K}^{\mathcal{D}}$, and the coefficients, $C^{\mathcal{D}}$, depend on a specific diagram topology. The final summation over the set of $\{\ell_i\}$ can be linearized such that the result of the diagram is a simple dot-product.

In summary, by using the DLR representation in a fixed basis, we are able to extract a factorizable component of the problem that only depends on the choice of the DLR basis which we refer to as the computation kernel. The computation kernel can be evaluated for any particular diagram via algorithmic Matsubara integration in a symbolic form, which can then be evaluated for a choice of external frequencies and inverse temperatures where each result is a single complex-valued number. If one stores those results as a function of the sets of DLR pole indices, $\{\ell_i\}$, then, via Eq. (10), one only needs to generate the coefficients to evaluate the diagram. Since all problem specific information is contained in the coefficients, the kernel is reusable for distinct physical problems. The computational effort to compute any diagram for any physical problem is then only the evaluation of the non-temporal degrees of freedom which appear as products of the DLR tensor and interaction matrix elements. We highlight that, while distinct, the present work has connections with a number of important research advancements including: overcomplete representations, partial spectral functions, and tensor trains.[10, 13, 37–39]

III. PROBLEM SPECIFIC APPLICATION

We demonstrate a minimal application of the computation kernel approach of Eq. (10). We solve two model Hamiltonians: a two-band impurity with a general 4-index interaction tensor, and a lattice problem, the Hubbard Hamiltonian on the 2D square lattice. We will restrict ourselves to the evaluation of a single second-order self energy diagram. We emphasize that the goal is not to extract physically relevant information about these model systems but to demonstrate that the construction of a single computational kernel, $\mathcal{K}_{i\nu_x, \beta}^{(2)}(\{\ell_i\})$, will allow us to evaluate the full result of these two very different physical systems.

A. Hamiltonians

1. Multi-band Impurities

We will evaluate diagrams for a very general two-body Hamiltonian with two terms; a single-particle term, H_0 , and a generalized four-operator interaction term, H_V . These are given by

$$H = \underbrace{\sum_{ab} h_{ab} c_a^\dagger c_b}_{H_0} + \frac{1}{2} \underbrace{\sum_{abcd} U_{abcd} c_a^\dagger c_c^\dagger c_d c_b}_{H_V}. \quad (11)$$

Here a and b are arbitrary band indices and the c_i^\dagger and c_i represent standard creation and annihilation operators in the state i , respectively, and the values of h_{ab} represent one-electron integrals while U_{abcd} is the two-electron interaction matrix. We will use the H₂ atom

at equilibrium separation in the sto-6G basis as a test case. We obtain the single-particle matrix h_{ab} based on the restricted Hartree-Fock approximation and the two-electron coulomb integrals U_{abcd} both in the molecular orbital basis in units of hartrees using the `pyscf` package[40]. Values used for h_{ab} and U_{abcd} are included in the supplementary files.

2. Hubbard Hamiltonian on a Lattice

We study the single-band Hubbard Hamiltonian on a 2D square lattice[41],

$$H = \sum_{ij\sigma} t_{ij} c_{i\sigma}^\dagger c_{j\sigma} + U \sum_i n_{i\uparrow} n_{i\downarrow}, \quad (12)$$

where t_{ij} is the hopping amplitude, $c_{i\sigma}^{(\dagger)}$ ($c_{i\sigma}$) is the creation (annihilation) operator at site i , $\sigma \in \{\uparrow, \downarrow\}$ is the spin, U is the onsite Hubbard interaction, and $n_{i\sigma} = c_{i\sigma}^\dagger c_{i\sigma}$ is the number operator. We restrict the sum over sites to nearest neighbors for a 2D square lattice, resulting in the free particle energy

$$\epsilon(\mathbf{k}) = -2t[\cos(k_x) + \cos(k_y)] - \mu,$$

where μ is the chemical potential, and t is the nearest-neighbor hopping amplitude. We work with energies in units of the hopping, $t = 1$. We absorb the Hartree shift and restrict our discussion to the $\mu = 0$, half-filled case.

B. Computation Kernel for Second Order Self Energy

We will evaluate the second order self-energy diagram, $\Sigma^{(2)}$, given by

$$\Sigma^{(2)} = \sum_{i\nu_1, i\nu_2} \sum_{\{a_j b_j\}} G_{a_1 b_1}(i\nu_1) G_{a_2 b_2}(i\nu_2) G_{a_3 b_3}(i\nu_1 - i\nu_2 + i\nu_x) \bar{U}, \quad (13)$$

where we maintain the subscript notation of Eq. (11). We will need to interpret the summation over the internal subscripts $a_1 b_1$, $a_2 b_2$, and $a_3 b_3$ for the physical problem being solved and choose a labelling scheme for the diagram. The labelling we will work with is presented in Fig. 2. We evaluate the kernel, $\mathcal{K}_{i\nu_n, \beta}^{(2)}(\{\ell\})$, for this diagram at a particular inverse temperature β for a range of frequencies. Specifically we obtain the kernel for the first 10 Matsubara frequencies at a dimensionless $\beta = 5$. We place the DLR basis poles and the results of the full kernel in the supplemental files where for each $i\nu_n$ the kernel is a list of complex numbers for a particular choice of basis. We have chosen 3 unique DLR representations using

$\Lambda = 5.15, 5.2$, and 5.5 and an error tolerance of $\epsilon \approx 10^{-7}$ at $\beta = 5$. The DLR[34] then generates 3 sets of 16 poles, x_{ℓ_1} , x_{ℓ_2} , and x_{ℓ_3} , which represent the non-physical space used to generate the kernel $\mathcal{K}_{i\nu_n, \beta}^{(2)}(\{\ell\})$. We generate the kernel using AMI but note that the analytic result can be obtained easily by hand[32]. We emphasize that we are now going to use this one kernel to compute the two distinct physical problems described above.

In the case of the 2D square lattice Hubbard model (Eq. (12)), the non-interacting Green's function is evaluated on an $L \times L$ grid in k_x and k_y and used to generate the DLR coefficients $A_{a_j b_j}^{\ell_j}$. In this case, a_j and b_j are diagonal states and these indices are reinterpreted to refer

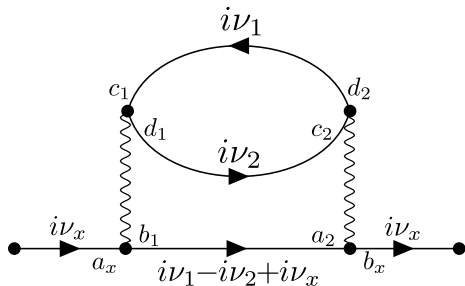


FIG. 2. Labelled second order self-energy diagram, $\Sigma^{(2)}$. The diagram has external frequency, $i\nu_x$, and external band-indices a_x and b_x . Internal band indices are arbitrarily assigned to simplify the form of the interaction matrix elements.

to the k_x and k_y coordinates respectively while the interaction amplitudes are given simply by $\bar{U} = U^2$. Hence, we need to obtain the coefficients

$$C_{\beta, k_x, k_y}^{(2)}(\{\ell_i\}) = \sum_{\substack{k_{1x}, k_{1y} \\ k_{2x}, k_{2y}}} A_{a_1 b_1}^{\ell_1} A_{a_2 b_2}^{\ell_2} A_{a_3 b_3}^{\ell_3} U^2. \quad (14)$$

The relation between the subscripts and internal momenta are not unique and we have selected the labelling $a_1, b_1 = k_{1x}, k_{1y}$, $a_2, b_2 = k_{2x}, k_{2y}$, and $a_3, b_3 = k_{1x} - k_{2x} + k_x, k_{1y} - k_{2y} + k_y$ in order to match the definitions of the independent and dependent Matsubara frequencies.

We perform the summation of the internal momenta grids for each ℓ_1, ℓ_2 , and ℓ_3 to obtain the total weights. The distribution of those weights can be refined by increasing L , and while this increases the geometry of the $A_{a_j b_j}^{\ell_j}$ coefficients it does not change the geometry of the resulting $C^{(2)}(\{\ell_i\})$ coefficients, and so the same kernel $\mathcal{K}_{i\nu_n, \beta}^{(2)}(\{\ell\})$ can be used.

In the case of the multi-band impurity problem (Eq. (11)) the coefficients $a_j b_j$ represent diagonal and off-diagonal Green's function matrix element indices. We do a single shot calculation starting from a diagonal Green's function, but write the coefficient without assuming they are diagonal and also include the interaction matrix elements $\bar{U} = U_{a_1 b_1 c_1 d_1} U_{a_2 b_2 c_2 d_2}$. We assign specific labels to the $a_j b_j$ indices in Fig. 2 and specify which indexes are external lines of the diagram. This results in

$$C_{\beta, a_x, b_x}^{(2)}(\{\ell_i\}) = \sum_{\substack{\{a_1 b_1 c_1 d_1\} \\ \{a_2 b_2 c_2 d_2\}}} A_{d_2 c_1}^{\ell_1} A_{d_1 c_2}^{\ell_2} A_{b_1 a_2}^{\ell_3} \\ \times U_{a_1 b_1 c_1 d_1} U_{a_2 b_2 c_2 d_2} \delta_{a_1 a_x} \delta_{b_2 b_x}. \quad (15)$$

We will apply this to a two band toy problem, but this expression is valid for any number of bands for a choice of a_x, b_x . We notice that in both Eqns. (14) and (15) the coefficients depend on the choice of inverse temperature β and also any external spatial degrees of freedom of the system. As is the case in lattice problems that a variety

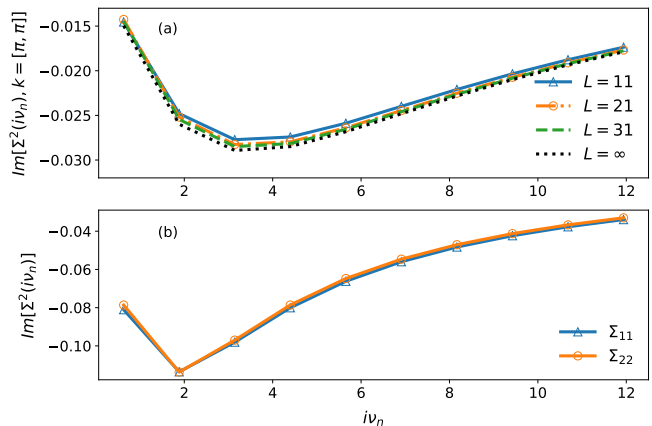


FIG. 3. The imaginary part of the second order self energy for the first 10 Matsubara frequencies at $\beta = 5$ utilizing a precomputed computation kernel for the diagram. (a) The 2D Hubbard result for external momentum $k_x = (\pi, \pi)$ at $U/t = 1$ for the $L \times L$ system with $L = 11, 21$, and 31 . Also included is a benchmark reference for the $L \rightarrow \infty$ limit. (b) The H₂ molecule for the sto-6G basis which exhibits only diagonal elements of the self-energy.

of distinct $L \times L$ grids could be used while invoking the same Kernel, the choice of the molecular basis also does not impact the use of the same kernel, $\mathcal{K}_{i\nu_n, \beta}^{(2)}(\{\ell\})$. The kernel is truly universal and can be used to generate the solution for the second order self energy diagram for any physical problem.

As a demonstration of the utility of the approach, we plot the second order self-energy for our two toy problems in Fig. 3. The results are obtained via Eq. (10) where the same computation kernel is used for both physically distinct problems. In the case of the Hubbard model, we choose a single point in the Brillouin zone at an external momentum of $k_x = (\pi, \pi)$. Since we only need to compute $C_{\beta, k_x, k_y}^{(2)}$ it is straightforward to probe increasing system sizes at an expense of $\mathcal{O}(L^{md})$, where $m = 2$ is the expansion order and d is the spatial dimensionality. Results for $L = 11, 21$, and 31 are shown as well as a benchmark for the thermodynamic $L \rightarrow \infty$ limit, obtained from continuous stochastic integration methods. We emphasize that the results are well behaved and systematically approach the TL benchmark result. For each choice of L the approach is a virtually exact numerical evaluation of the finite-size problem, where the only uncertainty comes from the DLR fit of the original coefficients and the details of how that uncertainty propagates into the kernel. In all cases explored, the uncertainty is exponentially suppressed, and since we have selected a DLR representation with an error tolerance of $\epsilon \approx 10^{-7}$ the error in these results is completely negligible on this scale. Deviation from the $L \rightarrow \infty$ result is due only to finite-size effects. In Fig. 3(b) we present the diagonal terms of the self-energy for the H₂ molecule. The coefficients $C_{\beta, a_x, b_x}^{(2)}(\{\ell_i\})$ are obtained via Eq. (15) and

then the self energy is generated using the same kernel as for the Hubbard Hamiltonian. Since the two molecular states h_{11} and h_{22} are not energetically symmetric, there are expected to be small differences between the two curves. Unlike the lattice problem there are no additional spatial degrees of freedom and so the result is exact for this choice of basis. One could choose to represent the H_2 molecule in a more complex basis, and while this increases the numerical expense of evaluating Eq. (15) the computation kernel is unaffected.

The problems solved here have little in common. We are not interested in the specific result for either problem as they can be straightforwardly verified. Instead, we emphasize that we have a single kernel from which accurate results for the selected diagram can be obtained by only evaluating a trivially parallelizable sum of products of A_{ab}^ℓ coefficients. Since this same procedure can be applied to any diagram the potential applications of this approach are endless. For transparency, the full details of the kernel $\mathcal{K}_{i\nu_n,\beta}^{(2)}(\{\ell\})$ are provided in the supplementary files along with the problem specific coefficients for each curve in the figure.

IV. DISCUSSION AND CONCLUSIONS

We have applied the discrete Lehmann representation to Feynman diagrams comprised of matrix-valued Green's functions. This process replaces the physical computational space with an exponentially larger, auxiliary computational space defined by an arbitrary choice of DLR poles. The byproduct of this implicit over-fitting of the Green's function is that in the non-physical space, the temporal and spatial integrations completely decouple. The temporal integrals become equivalent to a multi-band impurity problem that can be treated exactly, for a given diagram, via algorithmic Matsubara integration. The spatial integrals are simplified into simple sums and products of complex numbers that are known, and arise from the DLR fitting procedure. The key result of this methodology is the ability to precompute the computation kernel a single time and reuse it for alternate physical problems. Once the computation kernel is obtained for a set of external frequencies and temperatures, it can be used to solve that same diagram for any physical problem. Solving any new physical problem requires only the solution to the spatial components of the diagram that, in the computation kernel approach, will always appear as a product of known tensor elements. This represents

a drastic reduction in complexity for solving correlated electron problems.

Whether or not there is computational advantage to this approach has yet to be demonstrated. Since the scaling properties are highly problem specific, we discuss the scaling of the computation kernel, $\mathcal{K}^{\mathcal{D}}$. For a single diagram the evaluation of the temporal integrals via AMI has a nearly factorial scaling, $\mathcal{O}(m!)$, with expansion order, m . Invoking the computation kernel representation results in exponential scaling in the DLR basis size times the original factorial, $\mathcal{O}(\ell_i^{am}m!)$, where a is a diagram-dependent constant. With the computation kernel approach it is conceivable that paying the more expensive $\mathcal{O}(\ell_i^{am}m!)$ price solves the kernel once and for all for a given diagram. This leads to the potential that all future evaluations require only $\mathcal{O}(\ell_i^{am})$ evaluations to perform the final products of Eq. (10). There is however an exponential growth of computational expense for determining the spatial integrals and if any advantage is to be found remains to be explicitly shown. Nevertheless, the method we present allows for fully self-consistent perturbative approaches that were not previously possible for arbitrary problems, as was already demonstrated for impurity problems with no spatial integrals in Ref. [32]. The same self-consistent procedures apply here, where on each step of the self-consistency there is no change to the computation kernel and one simply updates the coefficients $C^{\mathcal{D}}$ to reflect updates to the DLR fit coefficients $A_{a_j b_j}^{\ell_j}$.

Finally, when one takes a step back from the details of the math there is a simple message in this work. Abstracting the physical space of poles to a reusable, computational space introduces the possibility of exciting, practical applications. By having the kernel contain none of the problem specific information, caching or generating a repository of kernels has the potential to reduce computation costs and generate high quality data to a tunable degree of accuracy either as inputs or to validate the predictions of large quantitative models. Large quantitative models (LQMs) require massive amounts of accurate numerical data and are increasingly used to analyze, predict and simulate complex systems.[42] The applications of LQMs range from new material discovery for use in batteries and catalysis reactions to genomics research where binding affinities, molecular design and protein-ligand interactions have the potential to revolutionize drug design. Although more code development is needed in order to apply the computation kernel to this broad spectrum of problems, our approach appears to be a promising avenue for future research.

[1] D. Wu, R. Rossi, F. Vicentini, N. Astrakhantsev, F. Becca, X. Cao, J. Carrasquilla, F. Ferrari, A. Georges, M. Hibat-Allah, M. Imada, A. M. Läuchli, G. Mazzola, A. Mezzacapo, A. Millis, J. R. Moreno, T. Neupert,

Y. Nomura, J. Nys, O. Parcollet, R. Pohle, I. Romero, M. Schmid, J. M. Silvester, S. Sorella, L. F. Tocchio, L. Wang, S. R. White, A. Wietek, Q. Yang, Y. Yang, S. Zhang, and G. Carleo, Variational benchmarks for

- quantum many-body problems, *Science* **386**, 296 (2024), <https://www.science.org/doi/pdf/10.1126/science.adg9774>.
- [2] T. Louvet, T. Ayral, and X. Waintal, On the feasibility of performing quantum chemistry calculations on quantum computers (2024), arXiv:2306.02620 [quant-ph].
 - [3] M. Qin, T. Schäfer, S. Andergassen, P. Corboz, and E. Gull, The hubbard model: A computational perspective, *Annual Review of Condensed Matter Physics* **13**, 275 (2022).
 - [4] R. Rossi, F. Werner, N. Prokof'ev, and B. Svistunov, Shifted-action expansion and applicability of dressed diagrammatic schemes, *Phys. Rev. B* **93**, 161102 (2016).
 - [5] R. Rossi, Determinant diagrammatic monte carlo algorithm in the thermodynamic limit, *Phys. Rev. Lett.* **119**, 045701 (2017).
 - [6] F. Šimkovic and E. Kozik, Determinant monte carlo for irreducible feynman diagrams in the strongly correlated regime, *Phys. Rev. B* **100**, 121102 (2019).
 - [7] E. Kozik, M. Ferrero, and A. Georges, Nonexistence of the luttinger-ward functional and misleading convergence of skeleton diagrammatic series for hubbard-like models, *Phys. Rev. Lett.* **114**, 156402 (2015).
 - [8] H. Eßl, M. Reitner, E. Kozik, and A. Toschi, How to stay on the physical branch in self-consistent many-electron approaches (2025), arXiv:2502.01420 [cond-mat.str-el].
 - [9] B. D. E. McNiven, G. T. Andrews, and J. P. F. LeBlanc, Single particle properties of the two-dimensional hubbard model for real frequencies at weak coupling: Breakdown of the dyson series for partial self-energy expansions, *Phys. Rev. B* **104**, 125114 (2021).
 - [10] M. K. Ritter, Y. Núñez Fernández, M. Wallerberger, J. von Delft, H. Shinaoka, and X. Waintal, Quantics tensor cross interpolation for high-resolution parsimonious representations of multivariate functions, *Phys. Rev. Lett.* **132**, 056501 (2024).
 - [11] A. Erpenbeck, W.-T. Lin, T. Blommel, L. Zhang, S. Iskakov, L. Bernheimer, Y. Núñez Fernández, G. Cohen, O. Parcollet, X. Waintal, and E. Gull, Tensor train continuous time solver for quantum impurity models, *Phys. Rev. B* **107**, 245135 (2023).
 - [12] Y. N. Fernández, M. K. Ritter, M. Jeannin, J.-W. Li, T. Kloss, T. Louvet, S. Terasaki, O. Parcollet, J. von Delft, H. Shinaoka, and X. Waintal, Learning tensor networks with tensor cross interpolation: new algorithms and libraries (2024), arXiv:2407.02454 [physics.comp-ph].
 - [13] S. Rohshap, M. K. Ritter, H. Shinaoka, J. von Delft, M. Wallerberger, and A. Kauch, Two-particle calculations with quantics tensor trains – solving the parquet equations (2024), arXiv:2410.22975 [cond-mat.str-el].
 - [14] H. Shinaoka, N. Chikano, E. Gull, J. Li, T. Nomoto, J. Otsuki, M. Wallerberger, T. Wang, and K. Yoshimi, Efficient ab initio many-body calculations based on sparse modeling of Matsubara Green's function, *SciPost Phys. Lect. Notes* , 63 (2022).
 - [15] S. Dirnböck, S.-S. B. Lee, F. B. Kugler, S. Huber, J. von Delft, K. Held, and M. Wallerberger, Overcomplete intermediate representation of two-particle green's functions and its relation to partial spectral functions, *Phys. Rev. Res.* **6**, 043228 (2024).
 - [16] J. Kaye, K. Chen, and O. Parcollet, Discrete lehmann representation of imaginary time green's functions, *Phys. Rev. B* **105**, 235115 (2022).
 - [17] D. Kiese, H. U. R. Strand, K. Chen, N. Wentzell, O. Parcollet, and J. Kaye, Discrete lehmann representation of three-point functions, *Phys. Rev. B* **111**, 035135 (2025).
 - [18] J. Otsuki, M. Ohzeki, H. Shinaoka, and K. Yoshimi, Sparse modeling in quantum many-body problems, *Journal of the Physical Society of Japan* **89**, 012001 (2020), <https://doi.org/10.7566/JPSJ.89.012001>.
 - [19] J. Vučićević and M. Ferrero, Real-frequency diagrammatic monte carlo at finite temperature, *Phys. Rev. B* **101**, 075113 (2020).
 - [20] J. Vučićević, P. Stipsić, and M. Ferrero, Analytical solution for time integrals in diagrammatic expansions: Application to real-frequency diagrammatic monte carlo, *Phys. Rev. Res.* **3**, 023082 (2021).
 - [21] J. Kovačević, M. Ferrero, and J. Vučićević, Towards numerically exact computation of conductivity in the thermodynamic limit of interacting lattice models (2025), arXiv:2501.19118 [cond-mat.str-el].
 - [22] A. Taheridehkordi, S. H. Curnoe, and J. P. F. LeBlanc, Algorithmic matsubara integration for hubbard-like models, *Phys. Rev. B* **99**, 035120 (2019).
 - [23] A. Taheridehkordi, S. H. Curnoe, and J. P. F. LeBlanc, Algorithmic approach to diagrammatic expansions for real-frequency evaluation of susceptibility functions, *Phys. Rev. B* **102**, 045115 (2020).
 - [24] A. Taheridehkordi, S. H. Curnoe, and J. P. F. LeBlanc, Optimal grouping of arbitrary diagrammatic expansions via analytic pole structure, *Phys. Rev. B* **101**, 125109 (2020).
 - [25] I. Assi and J. P. F. LeBlanc, Symbolic determinant construction of perturbative expansions, *Phys. Rev. B* **109**, 125143 (2024).
 - [26] B. D. E. McNiven, H. Terletska, G. T. Andrews, and J. P. F. LeBlanc, One- and two-particle properties of the weakly interacting two-dimensional hubbard model in proximity to the van hove singularity, *Phys. Rev. B* **106**, 035145 (2022).
 - [27] R. Farid, M. Grandadam, and J. P. F. LeBlanc, Pairing susceptibility of the two-dimensional hubbard model in the thermodynamic limit, *Phys. Rev. B* **107**, 195138 (2023).
 - [28] R. Farid and J. P. F. LeBlanc, Pairing susceptibility in the weakly interacting multilayer hubbard model evaluated by direct perturbative expansion, *Phys. Rev. B* **110**, 144511 (2024).
 - [29] J. P. F. LeBlanc, K. Chen, K. Haule, N. V. Prokof'ev, and I. S. Tupitsyn, Dynamic response of an electron gas: Towards the exact exchange-correlation kernel, *Phys. Rev. Lett.* **129**, 246401 (2022).
 - [30] D. Gazizova and J. P. F. LeBlanc, Emergent nearest-neighbor attraction in the fully renormalized interactions of the single-band repulsive hubbard model at weak coupling, *Phys. Rev. B* **108**, 165149 (2023).
 - [31] M. D. Burke, M. Grandadam, and J. P. F. LeBlanc, Renormalized perturbation theory for fast evaluation of feynman diagrams on the real frequency axis, *Phys. Rev. B* **107**, 115151 (2023).
 - [32] D. Gazizova, L. Zhang, E. Gull, and J. P. F. LeBlanc, Feynman diagrammatics based on discrete pole representations: A path to renormalized perturbation theories, *Phys. Rev. B* **110**, 075158 (2024).
 - [33] J. Kaye, K. Chen, and H. U. R. Strand, *Comp. Phys. Comm.* **280**, 108458 (2022).
 - [34] J. Kaye, H. U. r. Strand, and N. Wentzell, cppdlr: Imaginary time calculations using the discrete lehmann representation, *Journal of Open Source Software* **9**, 6297

- (2024).
- [35] H. Elazab, B. McNiven, and J. LeBlanc, Libami: Implementation of algorithmic matsubara integration, *Computer Physics Communications* **280**, 108469 (2022).
- [36] M. D. Burke and J. P. F. LeBlanc, Torchami: Generalized cpu/gpu implementation of algorithmic matsubara integration, arXiv , 2311.17189 (2023).
- [37] J. Halbinger, B. Schneider, and B. Sbierski, Spectral representation of Matsubara n-point functions: Exact kernel functions and applications, *SciPost Phys.* **15**, 183 (2023).
- [38] F. B. Kugler, S.-S. B. Lee, and J. von Delft, Multipoint correlation functions: Spectral representation and numerical evaluation, *Phys. Rev. X* **11**, 041006 (2021).
- [39] S. Dirnböck, S.-S. B. Lee, F. B. Kugler, S. Huber, J. von Delft, K. Held, and M. Wallerberger, Overcomplete intermediate representation of two-particle green's functions and its relation to partial spectral functions, *Phys. Rev. Res.* **6**, 043228 (2024).
- [40] Q. Sun, T. C. Berkelbach, N. S. Blunt, G. H. Booth, S. Guo, Z. Li, J. Liu, J. D. McClain, E. R. Sayfutyarova, S. Sharma, S. Wouters, and G. K.-L. Chan, Pyscf: the python-based simulations of chemistry framework, *WIREs Computational Molecular Science* **8**, e1340 (2018).
- [41] J. P. F. LeBlanc, A. E. Antipov, F. Becca, I. W. Bulik, G. K.-L. Chan, C.-M. Chung, Y. Deng, M. Ferrero, T. M. Henderson, C. A. Jiménez-Hoyos, E. Kozik, X.-W. Liu, A. J. Millis, N. V. Prokof'ev, M. Qin, G. E. Scuseria, H. Shi, B. V. Svistunov, L. F. Tocchio, I. S. Tupitsyn, S. R. White, S. Zhang, B.-X. Zheng, Z. Zhu, and E. Gull (Simons Collaboration on the Many-Electron Problem), Solutions of the two-dimensional hubbard model: Benchmarks and results from a wide range of numerical algorithms, *Phys. Rev. X* **5**, 041041 (2015).
- [42] J. Jumper, R. Evans, A. Pritzel, T. Green, M. Figurnov, O. Ronneberger, K. Tunyasuvunakool, R. Bates, A. Žídek, A. Potapenko, A. Bridgland, C. Meyer, S. A. A. Kohl, A. J. Ballard, A. Cowie, B. Romera-Paredes, S. Nikolov, R. Jain, J. Adler, T. Back, S. Petersen, D. Reiman, E. Clancy, M. Zielinski, M. Steinegger, M. Pacholska, T. Berghammer, S. Bodenstein, D. Silver, O. Vinyals, A. W. Senior, K. Kavukcuoglu, P. Kohli, and D. Hassabis, Highly accurate protein structure prediction with alphafold, *Nature* **596**, 583 (2021).